Marlow, J. J., Colocci, I., Jungbluth, S. P., Weber, N. M., Gartman, A., Kallmeyer, J. (2020): Mapping metabolic activity at single cell resolution in intact volcanic fumarole sediment. - FEMS Microbiology Letters, 367, 1, fnaa031.

https://doi.org/10.1093/femsle/fnaa031

Mapping metabolic activity at single cell resolution in intact volcanic fumarole sediment

Jeffrey J Marlow, Isabella Colocci, Sean P Jungbluth, Nils Moritz Weber, Amy Gartman, Jens Kallmeyer
FEMS Microbiology Letters, Volume 367, Issue 1, January 2020, fnaa031,
https://doi.org/10.1093/femsle/fnaa031

ABSTRACT

Interactions among microorganisms and their mineralogical substrates govern the structure, function and emergent properties of microbial communities. These interactions are predicated on spatial relationships, which dictate metabolite exchange and access to key substrates. To quantitatively assess links between spatial relationships and metabolic activity, this study presents a novel approach to map all organisms, the metabolically active subset and associated mineral grains, all while maintaining spatial integrity of an environmental microbiome. We applied this method at an outgassing fumarole of Vanuatu's Marum Crater, one of the largest point sources of several environmentally relevant gaseous compounds, including H_2O, CO_2 and SO_2. With increasing distance from the sediment-air surface and from mineral grain outer boundaries, organism abundance decreased but the proportion of metabolically active organisms often increased. These protected niches may provide more stable conditions that promote consistent metabolic activity of a streamlined community. Conversely, exterior surfaces accumulate more organisms that may cover a wider range of preferred conditions, implying that only a subset of the community will be active under any particular environmental regime. More broadly, the approach presented here allows investigators to see microbial communities 'as they really are' and explore determinants of metabolic activity across a range of microbiomes.

INTRODUCTION

Volcanic emissions are a major source of several climate-relevant atmospheric gases, and have been linked to dramatic episodes of environmental change throughout Earth's history (Kamo *et al*. 2003; Jones *et al*. 2017). Gases such as water vapor, carbon dioxide, sulfur dioxide and methane enter the atmosphere not only through eruptions, but also—and in some cases dominantly—through fumaroles located on volcano flanks that can be active over much longer periods (Hernández *et al*. 1998; Schwandner *et al*. 2004). At this interface between hot, chemically reduced fluids and cold, oxygenated atmospheric gas, zones of disequilibria may be exploited by microbial metabolism (Amend and Shock 2001). In this context, fumarole-hosted microbial communities are poised to substantially modulate the chemical species emerging from terrestrial hydrothermal/volcanic environments that enter the atmosphere.

We sought to understand microbial community dynamics at this interface—to evaluate how abundance and metabolic activity patterns depend on sediment depth and the mineralogical neighborhood with single cell spatial resolution. This approach could serve as a model for other environmental microbiomes, where retaining spatial information is a challenge. Microbial community activity is often interrogated via meta-omics analyses, which typically extract classes of biomolecules from a bulk sample, or single or multi-cell imaging and sequencing efforts, which separate biomass from its environmental context. In both cases,

the microscale spatial relationships between different organisms and the surfaces with which they may interact are lost.

However, microbe–microbe and microbe–mineral interactions are central determinants of evolutionary trajectories (Cordero *et al*. 2012; Andersen *et al*. 2015), niche development (Morton *et al*. 2017), and community structure, function and stability (Boetius *et al*. 2000; Wright, Konwar and Hallam 2012; Coyte, Schluter and Foster 2015). Microbe–microbe spatial relationships govern chemical communication (West *et al*. 2007), metabolite exchange (Romine *et al*. 2017), and competition for resources (Mitri, Clarke and Foster 2016). Microbe–mineral associations can enable electron transfer in both directions: members of lineages such as *Geobacter* and *Shewanella* off-load electrons onto iron or manganese (Lovley and Phillips 1988; Myers and Nealson 1988), while metal-oxidizing microbes can access electrons from mineral-associated iron to reduce soluble nitrate (Shelobolina *et al*. 2012). Conductive minerals may even be used to facilitate electron transfer between two species, as in an acetate-oxidizing, nitrate-reducing partnership that appears to use magnetite to accelerate the exchange of reducing equivalents (Kato, Hashimoto and Watanabe 2012).

To better illuminate spatial arrangements among organisms and minerals at the atmospheric interface of an outgassing fumarole, we developed a metabolic activity-based approach using bioorthogonal non-canonical amino acid tagging (BONCAT, Hatzenpichler *et al*. 2014) to visualize cells that made new proteins during a field incubation period. We embedded the sediment to maintain microscale spatial configurations and examined microbe-mineral associations between all cells as well as the anabolically active subset via fluorescence and electron microscopy. While our limited sampling opportunity in this extreme environment made a comparative study infeasible, the robust method for *in situ* metabolic activity assessment presented here reveals depth- and mineral-dependent patterns of microbial activity and offers a promising new approach for the detailed interrogation of environmental microbiomes.

MATERIALS AND METHODS

Study site

Field-based incubations were performed at a fumarole on the southwestern flank of Marum crater on Ambrym Island, Vanuatu. The crater is approximately 400 m deep and hosts a lava lake that has likely been active for much of the last 300 years (Nemeth and Cronin 2006; Németh and Cronin 2008). The active Ambrym volcanic complex is about 10 km^2 in size, contains a few actively degassing craters and accounts for a remarkable 5–9% of global subaerial H_2O, CO_2 and HCl emissions and 10–17% of SO_2, HF and HBr emissions (Allard *et al*. 2016a).

The sampled fumarole was located ∼8 m below the crater rim. During the course of our field deployment (July 7–13, 2018), no dramatic changes in fumarole fluxes were observed (assessments made qualitatively by eye, ∼10 times per day). The fumarole complex was also observed during a previous expedition in December 2014, and was selected for sampling because of its relatively high volume of gas output, longevity and accessibility. The fumarole had an opening ∼25 × 40 cm; its upslope boundary was marked by sediment-mantled boulders, and its downslope boundary comprised several centimeters of loosely consolidated sediment. The interior surface temperature ranged from 60.1 °C (± 0.3 °C SD) at the visible bottom to 52.9 °C (± 0.5 °C SD) at the incubation horizon and 46.9 °C (± 0.8 °C SD) just below the fumarole-surface interface (Fig. S1). All temperatures were measured by

infrared thermometer (Lasergrip 800, Etekcity Corp., Anaheim, CA); reported values were the average of 10 spot measurements at the same depth within the fumarole.

In situ incubation

To investigate the metabolically active fraction of fumarole-hosted microbes, BONCAT was deployed. In this approach, synthetic amino acids, such as *L*-homopropargylglycine (HPG) used here, are introduced to a microbial community in aqueous solution. HPG is incorporated by native methionyl-tRNA synthetases into growing peptides in a manner that does not substantially alter community composition or activity (Hatzenpichler et al. 2014, 2016), and downstream azide-alkyne click chemistry enables fluorescent detection of newly synthesized proteins (Sletten and Bertozzi 2009; Hatzenpichler and Orphan 2015).
The sediment on a ledge inside the fumarole was incubated for 24 hours with a solution of 50 µM HPG, dissolved in 0.22 µm filtered condensed fumarole steam and pre-heated to the ambient temperature of 52.9 °C (± 0.5 °C SD). 50 µM HPG was determined to be the optimal concentration in *E. coli* cultures (Fig. S2, Table S1), in keeping with previous environmental studies (Hatzenpichler *et al*. 2016), and was used here. To incubate the sediment, the bottom conical portion of a 50-mL Falcon tube was removed by sterile razor blade; the lid was taken off; and the tube was inverted and pressed down into the fumarole sediment until the cut off bottom of the tube was flush with the surface. Every 8 hours, 10 mL of 50 µM HPG solution was pipetted directly onto the area bounded by the cut-off Falcon tube. Two parallel incubations were set up; one was used to assess the bioavailable HPG that remained in the sediment after the incubation period, and the other was chemically fixed with paraformaldehyde, washed with filter-sterilized condensed fumarole steam, dehydrated in an ethanol series, and embedded in an acrylic resin. (For additional procedural details, please see the Supporting Information—Supplemental Methods).

Sample sectioning and staining

To expose embedded cells, the resin-impregnated sediment was sectioned with a diamond saw (Model 650, South Bay Technology, San Clemente, CA) using a PELCO diamond wafering blade (#812–332, Ted Pella, Inc., Redding, CA). (Only the top ~2 cm was effectively solidified in the resin, potentially due to insufficient curing time or inconsistent temperatures in the fumarole during the curing process.) Two parallel cuts were made down the z-axis in the center of the core, producing a 5-mm thick vertical transect of the top ~2 cm of the fumarole sediment. The exposed surface was incubated with the 5 µM BONCAT dye solution (Table S1) in an anoxic chamber for 60 minutes. The section was then removed from the chamber, washed three times with sterile PBS, incubated in 5x SYBR Green I (referred to throughout as 'SYBR green'; Life Technologies, ThermoFisher, Waltham, MA) in the dark at room temperature for 15 minutes, rinsed three times with sterile PBS, and left to air dry in the dark before imaging. As a control, homogenized fumarole sediment not incubated in HPG solution was processed in an identical way. After fixation, rinsing, ethanol dehydration, and embedding, the control sediment was sectioned and stained as described above.

Fluorescence microscopy

Fluorescence imaging was performed with a LSM 880 confocal laser scanning microscope (Zeiss, Oberkochen, Germany) using a gallium arsenide phosphide (GaAsP) detector, a 20x objective lens, and DI water immersion. Argon and DPSS lasers were used for excitation at 458, 488, 514 and 561 nm; the detected emission wavelengths for the SYBR green and Cy3 dyes were 510–561 nm and 564–669 nm, respectively. A third channel of reflected light from

the 488 nm laser was collected to link sample features between the confocal and electron microscope data sets.
All imaging was conducted through the Zen 2.3 SP1 program. Each frame was 1024 × 1024 pixels (with a pixel dwell time of 32.77 µsec and pixel size of 240 nm) and averaged over four line-based scans. Gain settings were determined to minimize background and nonspecific signal. In the SYBR channel, a master gain of 750 and digital gain of 1.2 were used; for the Cy3 channel these parameters were 650 and 1.0, respectively. Focus was adjusted manually for each field of view prior to image capture.
Electron microscopy and energy dispersive x-ray spectroscopy
Following fluorescence microscopy, electron microscopy images and energy-dispersive X-ray spectroscopy (EDS) elemental maps were acquired with the Zeiss Supra55VP field emission scanning electron microscope. See Supplemental Methods for further detail.

Image processing
After the collection of primary images, deconvolution and co-registration were performed in Fiji/ImageJ. We used the ImageJ DeconvolutionLab2 plugin with a point spread function derived from Zeiss' Zen program based on our customized imaging parameters, and five iterations of the Richardson-Lucy algorithm (Richardson 1972; Lucy 1974). Denoising and SEM-fluorescence image co-registration were achieved with the Despeckle and bUnwarpJ algorithms, respectively.
Organism numbers and distance relationships from the co-registered fluorescence and SEM imagery were assessed in Matlab R2018b (details on how organisms were designated are provided in the Supplemental Methods). Concentrations were determined by counting the number of organisms across a given 1000 µm vertical window and dividing that number by the associated volume of 1×10^{-7} cm^3. This volume was calculated using the x and y dimensions of the fluorescence microscopy footprint and the z dimension established by an average of the SYBR green and Cy3 signal transmission distances through the resin as shown in Fig. S3. After processing, the + HPG, +BONCAT dye, +SYBR green experimental sample produced 29.4 times as many SYBR-active green objects (all organisms) and 21.7 times as many Cy3-active red objects (anabolically active organisms) as the autoclave-sterilized, -HPG, +BONCAT dye, +SYBR green control treatment. In other words, there is a > 95% likelihood that any given organism is a valid object unattributable to experimental or imaging artifacts.
To calculate organism concentrations as a function of depth into the sediment, the 1000 µm vertical window was moved down-section with a sliding step of 1 µm. Cell abundances were normalized by the proportion of mineral volume or mineral surface area in the corresponding sliding window to determine how the availability of solid substrate or mineral–pore interfaces, respectively, could structure the community (Fig. 1B). In these datasets, only regions whose full 1000 µm sliding window included mineral area or mineral surfaces, as relevant, were included. To evaluate the relationship between depth and organism activity, the proportion of cells within a given sliding window that were metabolically active (e.g. contained at least one red pixel) was determined (Fig. 1C). The proportion of organism pixels that were also BONCAT-active—a value interpreted loosely as 'degree of activity'—was also plotted (Fig. 1C). For both activity-based metrics, only regions whose full window included at least one cell were plotted.
For organism–mineral distances, we calculated the shortest Euclidean distance from each organism's outer surface to the perimeter of a mineral and recorded the identity of that mineral (see 'X-Ray Diffraction' below). To exclude cells that had been dislodged during the

embedding and sectioning process, all cells more than 40 µm away from the nearest mineral were removed. This cutoff (which removed 2% of all organisms) was based on a distance histogram to determine outliers, and is well within biofilm thicknesses associated with mineral grains (Ye, Zhang and Sleep 2015). Values were grouped by mineral type and placed in 25 µm histogram bins (Fig. 2). To determine organism–organism distances, the shortest distance between the outer surface of one organism and the outer surface of its nearest neighbor was calculated for each organism. Please see the Supplemental Methods for additional details on calculations of organism–mineral grain distances, organism–organism distances and organism concentration as a function of depth.

X-Ray diffraction

X-ray diffraction (XRD) was performed using an X'Pert3 powder diffractometer by Panalytical; see Supplemental Methods for additional information.

Water analysis

Major inorganic anions (Cl^-, NO_2^-, PO_4^{3-}, NO_3^- and SO_4^{2-}) were analyzed by suppressed ion chromatography (IC). Major cations (Li^+, Na^+, K^+, Mg^{2+}, Ca^{2+} and NH_4^+) were analyzed by non-suppressed ion chromatography. To quantify those cations not covered by IC, we also measured the water sample by inductively coupled plasma-optical emission spectroscopy (ICP-OES), using the 5110 system of Agilent Technologies. To ensure full comparability between the IC and ICP-OES results, the IC standard was used as an internal standard. For those ions that were measured by both methods the results were within one standard deviation of each other. (See Supplemental Methods for further information.)

Microbial community analysis

High throughput sequencing of the V4 and V5 regions of the 16S rRNA gene was performed to assess the diversity and composition of the archaeal and bacterial communities from two replicate fumarole samples. DNA was extracted from 0.3 g of sample material using the PowerSoil DNA Isolation Kit (MoBio, Carlsbad, CA) with the supplied protocol. Following PCR validation (including positive and negative controls) with the 27F and 1492R primers (Weisburg *et al*. 1991), target regions were amplified using oligonucleotide primers 515yF (5'-GTGYCAGCMGCCGCGGTAA-3') (Parada, Needham and Fuhrman 2016) and 806bR (5'-GGACTACNVGGGTWTCTAAT-3') (Apprill *et al*. 2015). Purified amplicons were diluted to equal concentrations and were sequenced (2 × 250 bp) on an Illumina (San Diego, CA, USA) MiSeq sequencer at RTL Genomics (Lubbock, TX, USA).

Unpaired forward and reverse reads with primers removed were used as input into DADA2 (version 1.10.1; (Callahan *et al*. 2016)). Chimeric sequences were removed using the 'removeBimeraDenovo' script using the 'consensus' method. Taxonomic identification of sequences was performed using DECIPHER (version 2.10.2; (Wright 2016; Murali, Bhargava and Wright 2018)) and the provided 'SILVA_SSU_r132_March2018' database. Sample metadata and the SSU rRNA sequence files used in this study were submitted to the NCBI BioSample and Sequence Read Archive databases and are accessible via BioProject identifier PRJNA603648. See Supplemental Methods for full amplification and sequence analysis procedures.

RESULTS AND DISCUSSION

The approach developed here enables the visualization of biomass and its metabolically active subset in relation to other cells and mineral grains while maintaining the spatial fidelity of the mineral grains and their associated biomass. The overall density was 5.2×10^8

organisms per cm^3, consistent with the upper range—typically found within lower-temperature surface horizons—of other fumaroles (Alexandrino *et al*. 2011; Li *et al*. 2015). Of these, 30.7% were anabolically active (i.e. at least one pixel with SYBR green signal also had Cy3 signal), a value that is near the lower bound of a range of temperate forest soil microbiomes (Couradeau *et al*. 2019) and similar to the proportion of active organisms in energetically-constrained methane seep sediments (Hatzenpichler *et al*. 2016). On average, 63% ± 27% SD of an organism's SYBR pixels also displayed Cy3 signal above background levels.

The fluorescence microscopy transect revealed a decrease in organism abundance as a function of depth into the fumarole sediment (Fig. 1A,B). To determine if this trend was attributable to the presence of mineral grains or grain boundaries, organism abundance was normalized by mineral area and surface in each corresponding field of view. The decrease in biomass with increasing depth remained a robust trend (Fig. 1B). Linear and exponential regression analyses showed that, with an exponential fit, sediment depth accounted for 75.7% of the observed variance in organism abundance (Fig. S4a, Table S2). When abundance was normalized by mineral area and by mineral surfaces, sediment depth explained 44.8% and 50.5% of the observed variance, respectively. (See Table S2 for linear and exponential regression analyses, including 95% confidence intervals.) These results suggest that depth-dependent environmental factors—not simply the presence or absence of mineral grains and surfaces—were key determinants of cell abundance. The proportion of cells demonstrating anabolic activity through BONCAT-associated fluorescence exhibited a different trend, increasing with depth (linear regression $R^2 = 0.855$, Fig. 1C, S4b, Table S2). An estimate of each organism's degree of activity, taken as the percentage of SYBR-active pixels that were also Cy3-active, showed a weak correlation with depth ($R^2 = 0.395$, Fig. 1C, Table S2).

Taken together, these data reveal an ecosystem marked by abundant but largely dormant organisms in the top centimeter shifting to a sparser community with comparatively higher metabolic activity in the 1–2 cm horizon. This pattern is consistent with colonization potential and environmental variability. At the fumarole sediment surface, colonization via both wet and dry aerial deposition could account for higher microbial abundances (Herbold *et al*. 2014; Li *et al*. 2015; Reche *et al*. 2018), but several environmental factors—including temperature, sunlight, UV radiation and relative humidity—are likely more variable than in deeper horizons. Environmental variability promotes a 'boom-bust' dynamic that allows a greater diversity of inhabitants (Tucker and Fukami 2014) but ensures that a substantial subset of them will be dormant at any given time (Lennon and Jones 2011). Below the surface, more consistent conditions could be maintained by warm, upward-advecting vapor and shielding from overlying particles. Variance in organism abundance and metabolic activity not related to sediment depth could reflect other parameters such as pore space connectivity or localized hydraulic pressure gradients (Mendoza-Lera *et al*. 2017).

Inter-organism spatial relationships indicated a strong preference for associating with organisms of similar activity status. For 77.1% of active organisms, the nearest neighbor was also anabolically active; for 88.6% of inactive organisms, the nearest neighbor was inactive. This clustering may reflect small-scale niches that support independent metabolic activity, cross-feeding relationships, or the exchange of 'public goods'—energetically costly but broadly beneficial products such as secondary metabolites—between distinct organisms (West *et al*. 2006; Sieber, McInerney and Gunsalus 2012).

Putative mineral grain identification by quantitative EDS and XRD enabled a mineral-based analysis of colonization and activity patterns (Fig. 2). Most organisms (51.3%) were

associated with augite, a solid solution pyroxene mineral common in Vanuatu's mafic deposits (Eggins 1993). With increasing distance into augite grains, organism abundance decreased, with an R^2 value of 0.875 for the exponential regression from mineral surface inward (Table S2). The proportion of active organisms did not demonstrate a clear monotonic relationship with distance into augite grains (Table S2); however, from 700 µm inward, 81.4% of detected organisms had a positive BONCAT signal, indicating that select interior microhabitats created the niches most amenable to metabolic activity during the course of the incubation period. In the silica grain, both organism abundance and activity demonstrated bimodal patterns, with peaks around the mineral surface and the 400–600 µm interior region (Fig. 2C). The highest proportion of active constituents (58.1%) occurred between 425–450 µm into the grain, though our small sample size of silica minerals makes substantive generalizations difficult.

Overall grain-focused results may reflect the same relationship between environmental variability and relative activity we observed with respect to sediment depth: mineral interiors—more insulated from temperature and geochemical fluctuations than surfaces—can support particularly active communities. Augite may be more amenable to this partitioning than silica because of the former's metal cations, whose oxidation state and reactivity could vary with changing environmental parameters (Hoch, Reddy and Drever 1996), as well as its porous texture, which has been shown to correlate with microbial abundance in impact-shocked gneiss (Cockell *et al*. 2002).

To better understand the role of microorganisms in Marum fumarole sediments, we measured geochemical parameters of the condensed steam and conducted a 16S rRNA gene survey. The condensed steam had a pH of 5.38, and the most prominent ions, measured by ion chromatography and inductively coupled plasma mass spectrometry, were potassium (400 µM) and sodium (140 µM), chloride (490 µM), fluoride (20 µM) and sulfate (10 µM, see Table S3). The only detectable nitrogen species was nitrate (3 µM). DNA was extracted from two replicate samples recovered immediately adjacent to the incubated sediment and submitted for high-throughput 16S rRNA gene sequencing. The resulting data were processed with the DADA2 program (Callahan *et al*. 2016), yielding 116 exact sequence variants. Full abundances and phylogenetic identifications are provided in Tables S4 and S5; values provided below are average abundances across replicates.

Archaeal diversity was dominated by the *Thaumarchaea* (94%), which accounted for 33% of all sequences. *Thaumarchaea* have been found in high abundance at other fumaroles (Bendia *et al*. 2018; Cockell *et al*. 2019) and are frequently implicated in ammonia oxidation, which enables early colonization of challenging environments and drives nitrogen cycling (Kimble *et al*. 2018). *Group 1.1c Thaumarchaea* are frequently associated with acidic environments, where, due to the protonation of ammonia to ammonium, they may depend on urea hydrolysis for ammonia provisioning (Lu and Jia 2013). This reaction could be outsourced to *Chloroflexi* (whose *Ktedonobacteraceae* family accounted for 23% of our sequences) that produce ureases and can use oxidized nitrogen species (Hanada and Pierson 2006; Sorokin *et al*. 2012); a similar putative symbiosis was observed in an acidic orthoquartzite cave (Barton *et al*. 2014). Because Marum emissions are devoid of nitrogen compounds (Radebaugh *et al*. 2016; Allard et al. 2016a, 2016b), the ecosystem may be nitrogen-limited. Cyanobacterial lineages (most notably *Chlorogloeopsis*, 1.6% of our sequences) may play key roles as atmospheric nitrogen fixers (Young 1992), enabling other detected organisms to carry out nitrogen-associated metabolisms—such as ammonium oxidation (*Nitrosotaleaceae*), nitrification (*Nitrosomonadaceae*), and denitrification (*Burkholderiaceae*)—and preventing substantial accumulation of extracellular nitrogen

compounds. Indeed, low standing concentrations can reflect limiting metabolites, and the abundance and diversity of nitrogen-metabolizing lineages detected here points to a dynamic nitrogen-cycling community running on fumes.
Ktedonobacteraceae also includes lineages of CO-oxidizing spore formers that have been found in high abundance at geothermal sites in Hawaii (King and King 2014), Italy (Gagliano *et al*. 2016) and Antarctica (Soo *et al*. 2009). Given their well-established quiescence mechanism and the potentially intermittent supply of CO associated with Ambrym emissions (Allard *et al*. 2016b), such lineages could represent a portion of the inactive biomass we observed. Heterotrophic lineages including many *Gammaproteobacteria* (15% of sequences) and *C. calidirosea* (Lee *et al*. 2011) (7% of sequences) could also account for the inactive biomass, as organic matter input is likely rare and may exhibit temporal variability.
The small sample size presented here (attributable to remote and challenging field conditions) limits the universality of our results and interpretation. Nonetheless, by employing appropriate controls and lab-based procedural tests, we believe this work signifies a benchmark study demonstrating the use of 'in-place', correlative microscopic assessments to map metabolic activity and microbe-mineral associations in extreme environments. We also note the fundamental challenge in ensuring that microscale spatial arrangements have been unaltered throughout the experimental process, which involved several fluid replacement steps. However, given the high frequency of rain events and subsequent runoff into the fumarole, it is likely that the shear forces associated with the experimental protocol were within the range of those experienced naturally, and that the adherent cells we observed are representative of native microbiota.

CONCLUSION

At a fumarole associated with one of the world's largest point sources of several greenhouse gases, we observed a high abundance of organisms in the upper (0–2 cm) horizon, whose most prominent constituents likely participate in nitrogen fixation and subsequent cycling. With increasing depth into the sediment, organism abundance decreased but the proportion of metabolically active organisms increased. A similar trend was observed with distance into mineral grains: abundance decreased, and the communities with the highest proportion of active cells were several hundred micrometers interior. Our results suggest that more protected niches provide a stable environment that consistently sustains a subset of the community, while exterior surfaces accumulate more organisms whose activity is contingent upon specific, temporally inconsistent conditions. The work presented here demonstrates a novel approach for *in situ* measurement of metabolic activity within a single-cell resolution spatial context that can reveal fundamental principles of community structuring across a wide array of microbiomes.

ACKNOWLEDGEMENTS

We would like to thank True to Nature Limited and Ultimate Volcano Expeditions for facilitating field work and providing extensive logistical support. Roland Hatzenpichler and Rachel Spietz provided extensive feedback during method development, as well as helpful comments on earlier versions of this manuscript. JJM thanks Peter Girguis and the Girguis Lab for the use of equipment during the lab-based portion of this study, as well as the Harvard Center for Biological Imaging and the Harvard Center for Nanoscale Systems. JJM was supported through a Rolex Explorer Grant and funding provided by the Gordon and Betty Moore Foundation, Grant GBMF5999.

Conflict of interest statement. The authors declare that they have no conflict of interest.
References

References

Alexandrino M, Macías F, Costa R *et al.* A bacterial consortium isolated from an Icelandic fumarole displays exceptionally high levels of sulfate reduction and metals resistance. *Journal of hazardous materials* 2011;187:362–70.

Allard P, Aiuppa A, Bani P *et al.* Prodigious emission rates and magma degassing budget of major, trace and radioactive volatile species from Ambrym basaltic volcano, Vanuatu island Arc. *Journal of volcanology and geothermal research* 2016a;322:119–43.

Allard P, Burton M, Sawyer G *et al.* Degassing dynamics of basaltic lava lake at a top-ranking volatile emitter: Ambrym volcano, Vanuatu arc. *Earth and Planetary Science Letters* 2016b;448:69–80.

Amend JP, Shock EL. Energetics of overall metabolic reactions of thermophilic and hyperthermophilic Archaea and Bacteria. *FEMS microbiology reviews* 2001;25:175–243.

Andersen SB, Marvig RL, Molin S *et al.* Long-term social dynamics drive loss of function in pathogenic bacteria. *Proc Natl Acad Sci USA* 2015;112:10756.

Apprill A, McNally S, Parsons R *et al.* Minor revision to V4 region SSU rRNA 806R gene primer greatly increases detection of SAR11 bacterioplankton. *Aquatic Microbial Ecology* 2015;75:129–37.

Barton HA, Giarrizzo JG, Suarez P *et al.* Microbial diversity in a Venezuelan orthoquartzite cave is dominated by the Chloroflexi (Class Ktedonobacterales) and Thaumarchaeota Group I. 1c. *Frontiers in microbiology* 2014;5:615.

Bendia AG, Signori CN, Franco DC *et al.* A mosaic of geothermal and marine features shapes microbial community structure on deception Island Volcano, Antarctica. *Frontiers in Microbiology* 2018;9.

Boetius A, Ravenschlag K, Schubert CJ *et al.* A marine microbial consortium apparently mediating anaerobic oxidation of methane. *Nature* 2000;407:623.

Callahan BJ, McMurdie PJ, Rosen MJ *et al.* DADA2: high-resolution sample inference from Illumina amplicon data. *Nature methods* 2016;13:581.

Cockell CS, Harrison JP, Stevens AH *et al.* A low-diversity microbiota inhabits extreme terrestrial basaltic terrains and their fumaroles: implications for the exploration of Mars. *Astrobiology* 2019;19:284–99.

Cockell CS, Lee P, Osinski G *et al.* Impact-induced microbial endolithic habitats. *Meteoritics & Planetary Science* 2002;37:1287–98.

Cordero OX, Ventouras L-A, DeLong EF *et al.* Public good dynamics drive evolution of iron acquisition strategies in natural bacterioplankton populations. *Proceedings of the National Academy of Sciences* 2012;109:20059–64.

Couradeau E, Sasse J, Goudeau D *et al.* Probing the active fraction of soil microbiomes using BONCAT-FACS. *Nature Communications* 2019;10:2770.

Coyte KZ, Schluter J, Foster KR. The ecology of the microbiome: Networks, competition, and stability. *Science* 2015;350:663.

Eggins S. Origin and differentiation of picritic arc magmas, Ambae (Aoba), Vanuatu. *Contributions to Mineralogy and Petrology* 1993;114:79–100.

Gagliano A, Tagliavia M, D'alessandro W *et al.* So close, so different: geothermal flux shapes divergent soil microbial communities at neighbouring sites. *Geobiology* 2016;14:150–62.

Hanada S, Pierson BK. The family chloroflexaceae. *The Prokaryotes: Volume 7: Proteobacteria: Delta, Epsilon Subclass* 2006:815–42.

Hatzenpichler R, Connon SA, Goudeau D *et al.* Visualizing in situ translational activity for identifying and sorting slow-growing archaeal− bacterial consortia. *Proceedings of the National Academy of Sciences* 2016;113:E4069–78.

Hatzenpichler R, Orphan VJ. Detection of protein-synthesizing microorganisms in the environment via bioorthogonal noncanonical amino acid tagging (BONCAT). *Hydrocarbon and Lipid Microbiology Protocols*. Springer, 2015, 145–57.

Hatzenpichler R, Scheller S, Tavormina PL *et al.* In situ visualization of newly synthesized proteins in environmental microbes using amino acid tagging and click chemistry. *Environmental microbiology* 2014;16:2568–90.

Herbold CW, Lee CK, McDonald IR *et al.* Evidence of global-scale aeolian dispersal and endemism in isolated geothermal microbial communities of Antarctica. *Nature communications* 2014;5:3875.

Hernández PA, Pérez NM, Salazar JM *et al.* Diffuse emission of carbon dioxide, methane, and helium-3 from Teide Volcano, Tenerife, Canary Islands. *Geophysical Research Letters* 1998;25:3311–4.

Hoch A, Reddy M, Drever J. The effect of iron content and dissolved O2 on dissolution rates of clinopyroxene at pH 5.8 and 25 C: preliminary results. *Chemical Geology* 1996;132:151–6.

Jones DS, Martini AM, Fike DA *et al.* A volcanic trigger for the Late Ordovician mass extinction? Mercury data from south China and Laurentia. *Geology* 2017;45:631–4.

Kamo SL, Czamanske GK, Amelin Y *et al.* Rapid eruption of Siberian flood-volcanic rocks and evidence for coincidence with the Permian–Triassic boundary and mass extinction at 251 Ma. *Earth and Planetary Science Letters* 2003;214:75–91.

Kato S, Hashimoto K, Watanabe K. Microbial interspecies electron transfer via electric currents through conductive minerals. *Proceedings of the National Academy of Sciences* 2012;109:10042–6.

Kimble JC, Winter AS, Spilde MN *et al.* A potential central role of Thaumarchaeota in N-Cycling in a semi-arid environment, Fort Stanton Cave, Snowy River passage, New Mexico, USA. *FEMS Microbiol Ecol* 2018;94, DOI: 10.1093/femsec/fiy173.

King C, King G. Description of Thermogemmatispora carboxidivorans sp. nov., a carbon-monoxide-oxidizing member of the class Ktedonobacteria isolated from a geothermally heated biofilm, and analysis of carbon monoxide oxidation by members of the class Ktedonobacteria. *International journal of systematic and evolutionary microbiology* 2014;64:1244–51.

Lee KC-Y, Dunfield PF, Morgan XC *et al.* Chthonomonas calidirosea gen. nov., sp. nov., an aerobic, pigmented, thermophilic micro-organism of a novel bacterial class, Chthonomonadetes classis nov., of the newly described phylum Armatimonadetes originally designated candidate division OP10. *International journal of systematic and evolutionary microbiology* 2011;61:2482–90.

Lennon JT, Jones SE. Microbial seed banks: the ecological and evolutionary implications of dormancy. *Nature Reviews Microbiology* 2011;9:119.

Li H, Yang Q, Li J *et al.* The impact of temperature on microbial diversity and AOA activity in the Tengchong Geothermal Field, China. *Scientific Reports* 2015;5:17056.

Lovley DR, Phillips EJ. Novel mode of microbial energy metabolism: organic carbon oxidation coupled to dissimilatory reduction of iron or manganese. *Appl Environ Microbiol* 1988;54:1472–80.
Lu L, Jia Z. Urease gene-containing A rchaea dominate autotrophic ammonia oxidation in two acid soils. *Environmental microbiology* 2013;15:1795–809.
Lucy LB. An iterative technique for the rectification of observed distributions. *The astronomical journal* 1974;79:745.
Mendoza-Lera C, Frossard A, Knie M *et al.* Importance of advective mass transfer and sediment surface area for streambed microbial communities. *Freshwater biology* 2017;62:133–45.
Mitri S, Clarke E, Foster KR. Resource limitation drives spatial organization in microbial groups. *The ISME journal* 2016;10:1471.
Morton JT, Sanders J, Quinn RA *et al.* Balance Trees Reveal Microbial Niche Differentiation. Jansson JK (ed.). *mSystems* 2017;2:e00162-16.
Murali A, Bhargava A, Wright ES. IDTAXA: a novel approach for accurate taxonomic classification of microbiome sequences. *Microbiome* 2018;6:140.
Myers CR, Nealson KH. Bacterial manganese reduction and growth with manganese oxide as the sole electron acceptor. *Science* 1988;240:1319–21.
Nemeth K, Cronin SJ. Lava lakes and shallow level magmatic feeding systems of mafic volcanoes of an ocean island: Ambrym, Vanuatu (New Hebrides), South Pacific. 2006.
Németh K, Cronin SJ. Volcanic craters, pit craters and high-level magma-feeding systems of a mafic island-arc volcano: Ambrym, Vanuatu, South Pacific. *Geological Society, London, Special Publications* 2008;302:87–102.
Parada AE, Needham DM, Fuhrman JA. Every base matters: assessing small subunit rRNA primers for marine microbiomes with mock communities, time series and global field samples. *Environmental microbiology* 2016;18:1403–14.
Radebaugh J, Lopes RM, Howell RR *et al.* Eruptive behavior of the Marum/Mbwelesu lava lake, Vanuatu and comparisons with lava lakes on Earth and Io. *Journal of Volcanology and Geothermal Research* 2016;322:105–18.
Reche I, D'Orta G, Mladenov N *et al.* Deposition rates of viruses and bacteria above the atmospheric boundary layer. *The ISME journal* 2018;12:1154.
Richardson WH. Bayesian-based iterative method of image restoration. *JOSA* 1972;62:55–9.
Romine MF, Rodionov DA, Maezato Y *et al.* Underlying mechanisms for syntrophic metabolism of essential enzyme cofactors in microbial communities. *The ISME journal* 2017;11:1434.
Schwandner FM, Seward TM, Gize AP *et al.* Diffuse emission of organic trace gases from the flank and crater of a quiescent active volcano (Vulcano, Aeolian Islands, Italy). *Journal of Geophysical Research: Atmospheres* 2004;109.
Shelobolina E, Xu H, Konishi H *et al.* Microbial lithotrophic oxidation of structural Fe (II) in biotite. *Appl Environ Microbiol* 2012;78:5746–52.
Sieber JR, McInerney MJ, Gunsalus RP. Genomic insights into syntrophy: the paradigm for anaerobic metabolic cooperation. *Annual review of microbiology* 2012;66:429–52.
Sletten EM, Bertozzi CR. Bioorthogonal chemistry: fishing for selectivity in a sea of functionality. *Angewandte Chemie International Edition* 2009;48:6974–98.
Soo RM, Wood SA, Grzymski JJ *et al.* Microbial biodiversity of thermophilic communities in hot mineral soils of Tramway Ridge, Mount Erebus, Antarctica. *Environmental Microbiology* 2009;11:715–28.

Sorokin DY, Lücker S, Vejmelkova D *et al.* Nitrification expanded: discovery, physiology and genomics of a nitrite-oxidizing bacterium from the phylum Chloroflexi. *The ISME journal* 2012;6:2245.

Tucker CM, Fukami T. Environmental variability counteracts priority effects to facilitate species coexistence: evidence from nectar microbes. *Proceedings of the Royal Society B: Biological Sciences* 2014;281:20132637.

Weisburg WG, Barns SM, Pelletier DA *et al.* 16S ribosomal DNA amplification for phylogenetic study. *Journal of bacteriology* 1991;173:697–703.

West SA, Diggle SP, Buckling A *et al.* The social lives of microbes. *Annu Rev Ecol Evol Syst* 2007;38:53–77.

West SA, Griffin AS, Gardner A *et al.* Social evolution theory for microorganisms. *Nature reviews microbiology* 2006;4:597.

Wright ES. Using DECIPHER v2. 0 to analyze big biological sequence data in R. *R Journal* 2016;8.

Wright JJ, Konwar KM, Hallam SJ. Microbial ecology of expanding oxygen minimum zones. *Nature Reviews Microbiology* 2012;10:381.

Ye S, Zhang Y, Sleep BE. Distribution of biofilm thickness in porous media and implications for permeability models. *Hydrogeology journal* 2015;23:1695–702.

Young J. Phylogenetic classification of nitrogen-fixing organisms. *Biological nitrogen fixation* 1992;1544:43–86.

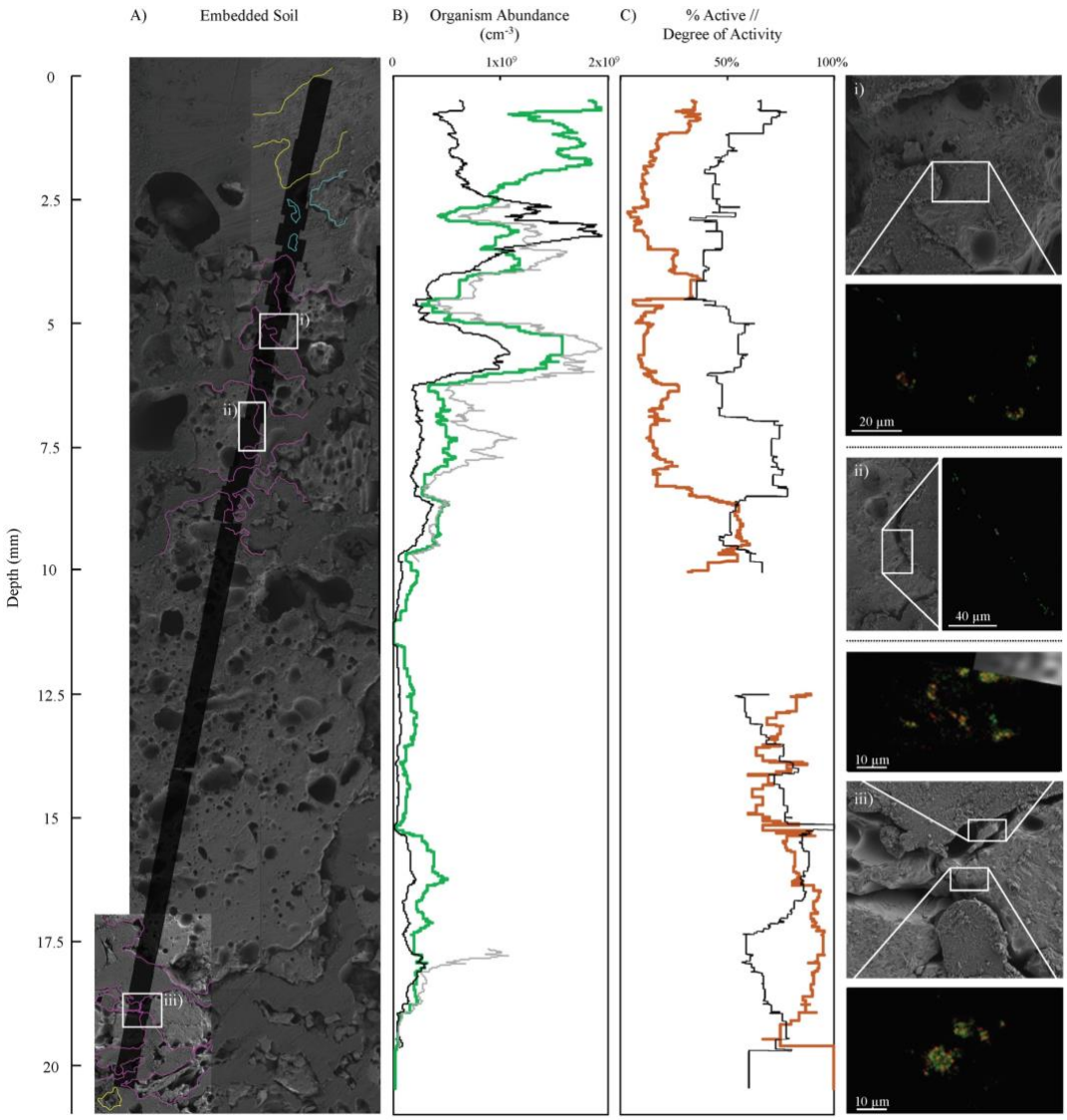

Figure 1. Mapping all cells and metabolically active cells along an embedded vertical transect of Marum fumarole sediment. A) Composite SEM image of the embedded sample. The black band shows the area of the fluorescence microscopy transect. Identified minerals are outlined for the transect portion that intersects the fluorescence analyses. Silica grains are outlined in yellow, augite grains in magenta and anorthite grains in cyan. Ai–iii) portions of the sediment sample at higher magnification, with the fluorescence images of the same field (green shows all SYBR-stained organisms and red indicates BONCAT-active organisms). B) Organism abundance with depth (green, r2 = 0.757), normalized by mineral grain volume (black, r2 = 0.505) and mineral grain surface area (grey, r2 = 0.448). C) Percentage of organisms that are active with depth (red, r2 = 0.855), and their degree of activity (black, r2 = 0.395). For B and C, plotted points indicate the data encompassed by a 1000 µm sliding window. Gaps in data reflect transect segments that did not produce a full 1000 µm window.

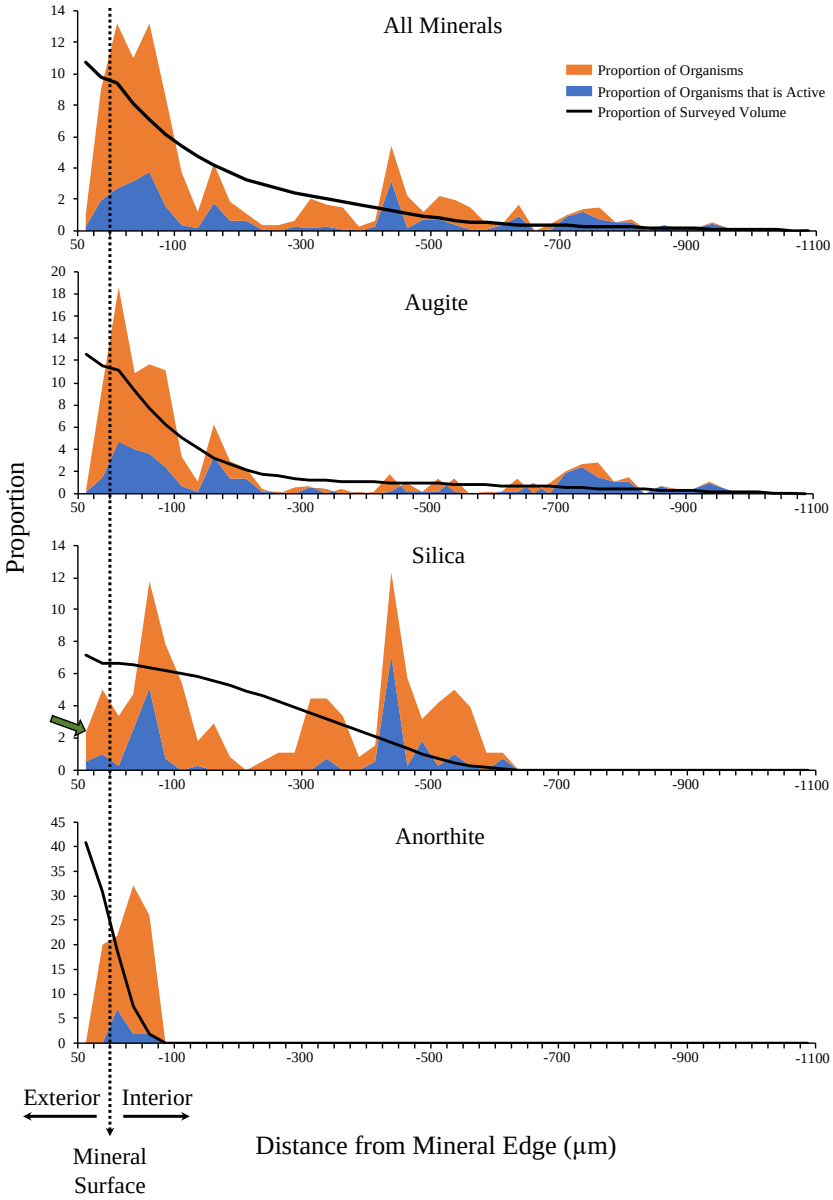

Histograms showing the location of all organisms and the active subset in relation to mineral surfaces for **A)** all minerals taken together, **B)** augite grains, **C)** silica grains and **D)** anorthite grains. The proportion of all organisms associated with each mineral type (*y*-axis) as a function of distance from the mineral grain surface (*x*-axis) is shown in orange. Each data point represents the value from a 25 µm bin, as indicated by the *x*-axis tick marks; negative distance values signify the mineral interior. The blue histogram indicates the fraction of all organisms detected in the corresponding 25 µm envelope that was metabolically active based on BONCAT fluorescence. For example, 2.4% of all organisms associated with silica were found between 25 and 50 µm outside the surface (see green arrow), as indicated by the first data point of the orange shading for silica. Of those organisms, 21.7% were found to be active, as indicated by the first data point of the blue shading, in relation to the orange, 'all organisms' data point. In this way, the blue shading indicates the proportion of metabolically active organisms among the subset of organisms found in each 25 µm bin (orange shading). (Given this presentation approach, values of orange data points across all histogram bins sum to 100%, but blue data points need not.) The black lines show the percentage of the surveyed fluorescence transect (from Fig. 1) for each mineral type that falls within the specified 25 µm bin. These values decrease with distance into the mineral, summing to a total of 100%.